

Two-dimensional simulation of a miniaturized inductively coupled plasma reactor

Sang Ki Nam and Demetre J. Economou^{a)}

Plasma Processing Laboratory, Department of Chemical Engineering, University of Houston, Houston, Texas 77204-4004

(Received 5 August 2003; accepted 5 December 2003)

A two-dimensional self-consistent simulation of a miniaturized inductively coupled plasma (mICP) reactor was developed. The coupled equations for plasma power deposition, electron temperature, and charged and neutral species densities, were solved to obtain the spatial distribution of an argon discharge. The effect of control parameters, such as power and pressure, on the evolution of plasma density and electron temperature was investigated. Strong ion density gradients were observed which can make spatially resolved Langmuir probe measurements particularly challenging. Simulation results were in reasonable agreement with available experimental data. The neutral gas temperature was predicted to be close to the wall temperature, due to the small length scale of the mICP, allowing for efficient heat transfer. © 2004 American Institute of Physics.
[DOI: 10.1063/1.1644043]

I. INTRODUCTION

Recently there has been interest in miniaturized plasma sources for use in microelectro-mechanical systems, miniature mass spectrometers, ion thrusters, plasma displays and gas sensors based on plasma emission (Refs. 1 and 2 and references therein). Miniaturized plasma sources include dc microhollow cathode discharges,³ ac plasma displays,⁴ microwave,⁵ and rf inductively coupled plasmas.^{1,2} Miniaturized inductively coupled plasmas (mICP) are a scaled down version of the ICPs used for large scale manufacturing of microelectronic devices.⁶ Due to their small size (\sim mm), several adjustments have to be made in the operating conditions of mICPs. For example, the gas pressure and the frequency of the plasma excitation field have to be increased, to be able to strike and sustain a plasma. An important difference between conventional ICPs and mICPs is the large surface-to-volume ratio of the latter. One of the consequences of this fact is that neutral gas heating is minimal in mICPs for the same volumetric power density (W/cm^3) as in conventional ICPs.

In this work, a two-dimensional simulation of a mICP was developed. The electromagnetic equation for the azimuthal electric field powering the plasma was solved simultaneously with the continuity equations for ion (electron) and neutral metastable argon density, and electron temperature. The model equations are described in Sec. II, and the method of solution is given in Sec. III. Results and discussion are presented in Sec. IV, including comparison with experimental data, while conclusions are summarized in Sec. V. A two-dimensional simulation of a microcell plasma in Xe for plasma display applications was presented by Kurihara and Makabe.⁴

II. MODEL FORMULATION

Figure 1 shows a schematic of a miniaturized cylindrical (5 mm radius and 6 mm length) inductively coupled plasma reactor,^{1,2} which can generate a high density plasma inside a chamber bounded by quartz and metal walls. The plasma is driven by a three-turn planar coil powered at UHF (450 MHz). The rf current in the coil produces a time-varying magnetic field, which in turn induces an azimuthal electric field heating the plasma electrons. The model consisted of an electromagnetic equation for the self-consistent azimuthal electric field powering the plasma, an equation for the electron temperature (assuming Maxwellian electrons), and mass continuity equations for the charged (Ar^+) and neutral (metastables, Ar^*) species. The model equations are described in the following sections. Details of the formulation may be found in published works.^{7,8} The electron density was calculated by charge neutrality (in this case it was identical to the ion density). This implies that the sheath near the reactor walls was not included in the simulation. The sheath is only 100 s of μm thick in the high density plasma. Due to the small dimensions of the source, the sheath thickness may be an appreciable fraction of the reactor dimension at low pressures and powers (small electron density). However, for typical operating conditions of this work, the sheath thickness was $\sim 250 \mu\text{m}$ and was neglected. The reaction set for argon (Table I) and the relevant reaction rate coefficients were the same as before.⁹

Assumptions and salient features of the model are enumerated below:

- (1) The fluid approximation was used since $\lambda/L=0.1$, where λ is the species mean-free path ($\sim 0.005 \text{ cm}$ at 1 Torr) and L is a characteristic dimension of the reactor ($\sim 0.5 \text{ cm}$).
- (2) The species densities, electron temperature, and induced electric field were assumed to be azimuthally symmetric [two-dimensional (2D), r - z system].

^{a)}Electronic mail: economou@uh.edu

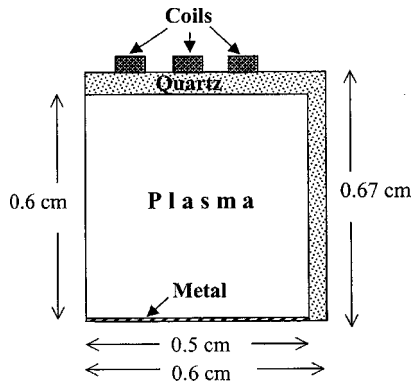


FIG. 1. Schematic of the miniaturized inductively coupled plasma system studied. Only half of the azimuthally symmetric system is shown.

(3) The charged particle flux was described by the drift-diffusion approximation (spatial inertia was neglected in the momentum equations) since the pressure was high enough for gas-phase collisions to dominate ion transport.

(4) The electron energy distribution function was assumed Maxwellian and an equation for the electron temperature was solved.

(5) Electron heating was assumed to be collisional (ohmic), since the effective electron mean free path was shorter than the thickness of the skin layer.^{10,11}

(6) Ions were assumed to be isothermal.

A. Electromagnetics

Under the assumption of azimuthally symmetric electric field, Maxwell's equations can be reduced to a single scalar equation in E_θ

$$\frac{1}{r} \frac{\partial}{\partial r} \left(r \frac{\partial E_\theta}{\partial r} \right) + \frac{\partial^2 E_\theta}{\partial z^2} - \frac{E_\theta}{r^2} + \frac{\omega^2}{c^2} K_c E_\theta = -j\omega\mu_0 J_\theta, \quad (1)$$

where ω is the driving frequency of the coil current, μ_0 is the vacuum permeability, K_c is the complex permittivity of the plasma (which depends on the electron density), J_θ is the impressed current density in the coils and c is the speed of light. At high frequencies, capacitive coupling may be important and the current can change along the coil.¹² A circuit model is then implemented to account for this effect, as outlined in Ref. 13. The power deposited in the plasma was computed by

$$P = \frac{1}{2} \text{Re}(\sigma_p) |E_\theta|^2, \quad (2)$$

where $\text{Re}(\sigma_p)$ is the real part of σ_p , the complex plasma conductivity. Equation (2) assumes that the power deposited in the plasma is due to ohmic heating. The conductivity was obtained from the following relations:

$$K_c = 1 - \frac{\omega_{pe}^2}{\omega^2 \left(1 + \frac{j\nu_m}{\omega} \right)}, \quad (3)$$

$$\sigma_p = -j\omega\epsilon_0(K_c - 1), \quad (4)$$

where

$$\omega_{pe}^2 = n_e e^2 / m \epsilon_0 \quad (5)$$

is the electron plasma frequency and ν_m is the electron momentum-exchange collision frequency.

The right-hand side of Eq. (1) includes only the current in the coil, J_θ . The (induced) current in the plasma is accounted for by the term involving the plasma permittivity K_c on the left-hand side of Eq. (1).

B. Ion transport and reaction

With the drift-diffusion flux approximation for the charged species, the continuity equation for positive ions (Ar^+) is of the form

$$\frac{\partial n_i}{\partial t} = -\nabla \cdot (z_i \mu_i n_i \vec{E}_{sc} - D_i \nabla n_i) + \sum_j R_{ji}, \quad (6)$$

where n_i , z_i , D_i , and μ_i are the positive ion density, charge number, diffusivity, and mobility, respectively. \vec{E}_{sc} is the electrostatic (space charge) field having two components (E_r and E_z). The summation on the right-hand side represents gas-phase reactions that produce (reactions R2, R3, and R6 of Table I) or destroy (none here) ions. Boundary conditions were $\vec{\Gamma}_i = 0$ on the symmetry axis/plane ($\vec{\Gamma}_i$ is the ion flux), and $n_i \approx 0$ on the walls due to the relatively high pressure. Thus, ions were lost by ambipolar diffusion to the walls. The electrostatic field was derived assuming no net current in the plasma.

$$\vec{E}_{sc} = \frac{D_i \nabla n_i - D_e \nabla n_e}{\mu_i n_i + \mu_e n_e}. \quad (7)$$

TABLE I. Reaction set used in the simulation (see Ref. 9).

Number	Process	Reaction	H_j (eV)
R1	Ground state excitation	$\text{Ar} + e \rightarrow \text{Ar}^* + e$	11.6
R2	Ground state ionization	$\text{Ar} + e \rightarrow \text{Ar}^+ + 2e$	15.7
R3	Step-wise ionization	$\text{Ar}^* + e \rightarrow \text{Ar}^+ + 2e$	4.1
R4	Superelastic collisions	$\text{Ar}^* + e \rightarrow \text{Ar} + e$	-11.6
R5	Metastable quenching	$\text{Ar}^* + e \rightarrow \text{Ar}^+ + e$	0.1
R6	Metastable pooling	$\text{Ar}^* + \text{Ar}^* \rightarrow \text{Ar}^+ + \text{Ar} + e$	
R7	Two-body quenching	$\text{Ar}^* + \text{Ar} \rightarrow 2\text{Ar}$	
R8	Three-body quenching	$\text{Ar}^* + 2\text{Ar} \rightarrow \text{Ar}_2 + \text{Ar}$	

The electron density n_e was obtained from quasineutrality as $n_e = n_i$.

C. Electron temperature

The electron energy equation reads

$$\frac{\partial}{\partial t} \left(\frac{3}{2} n_e T_e \right) = -\nabla \cdot \vec{q}_e + P - \sum_j R_{je} \Delta H_j, \quad (8)$$

with

$$\vec{q}_e = -K_e \nabla T_e + \frac{5}{2} \vec{\Gamma}_e T_e, \quad (9)$$

where T_e is the electron temperature (in electronvolts), \vec{q}_e is the electron energy flux, K_e is the electron thermal conductivity, and $\vec{\Gamma}_e$ is the electron flux. The second term on the right-hand side (RHS) represents the power deposited into the electrons [Eq. (2)]. The third term on the RHS represents the electron energy lost due to elastic and inelastic collisions. The boundary conditions were, $\vec{q}_e = 0$ on the symmetry axis/plane and $\vec{q}_e = 5/2 \vec{\Gamma}_e T_e$ along material boundaries.

D. Metastable transport and reaction

The Ar* metastable density was computed using Eq. (10) below assuming that transport is diffusion dominated

$$\frac{\partial n_*}{\partial t} = -\nabla \cdot (-D_* \nabla n_*) + \sum_j R_{j*} - \frac{n_*}{\tau_{\text{res}}}, \quad (10)$$

where R_{j*} represents reactions that produce or consume Ar*. A “composite” state was used to represent the long lived metastables (3P_0 and 3P_2 levels). Metastable reactions included production by excitation of ground state Ar (reaction R1 of Table I), and destruction by reactions R3–R8 of Table I. Reaction rate coefficients for metastable species were identical to those in Ref. 9. The last term in Eq. (10) accounts for convective flow losses of Ar* atoms through the residence time τ_{res} . Flow losses were negligible for the system at hand. The boundary conditions were zero gradient of density along the symmetry axis/plane ($\partial n_*/\partial r = 0$, $\partial n_*/\partial z = 0$), and $-D_* \nabla n_* = [\gamma/2(2-\gamma)] n_* v_*$ on walls, according to the Chantry¹⁴ boundary condition. Here D_* is the diffusivity of Ar* in Ar, γ is the destruction probability of Ar* atoms on walls (taken as unity), and v_* is their thermal velocity. Reaction rate coefficients for metastable species were identical to those in Ref. 9.

E. Neutral gas heating

Neutral gas heating has been found to be important in conventional ICPs.¹⁵ Since the power density in mICPs can be comparable to or larger than that in conventional ICPs, the effect of neutral gas heating in mICPs should be examined. The neutral gas temperature T_n (in K) can be computed by

$$\frac{\partial}{\partial t} \left(\frac{3}{2} N k_B T_n \right) = \nabla \cdot (k_n \nabla T_n) + \dot{Q}, \quad (11)$$

where N is the neutral gas density (by far ground state argon), k_n is the thermal conductivity of the gas, k_B is Boltz-

TABLE II. Base case operating parameters.

Pressure	500 mTorr
Plasma power	1.3 W
Frequency	450 MHz
Ar* wall “deactivation” probability	1
Ion temperature	300 K
Power absorption efficiency	2.5%

mann’s constant, and \dot{Q} is the power density ending up in heating the neutral gas. Boundary conditions on Eq. (11) are symmetry on axis and

$$-k_n \frac{\partial T_n}{\partial n} = h(T_n - T_w) \quad (12)$$

along the wall, where h is a heat transfer coefficient, and T_w is the wall temperature. When Eq. (11) is solved for a 1D parallel plate geometry (plate separation $2L$) using the symmetry condition at the center ($x=0$) and Eq. (12) on the wall ($x=L$), one obtains

$$T_n = \frac{1}{2} \frac{\dot{Q} L^2}{k_n} \left[1 - \left(\frac{x}{L} \right)^2 \right] + \frac{\dot{Q} L}{h} + T_w, \quad (13)$$

for a uniform heat generation term \dot{Q} . Thus, the gas temperature difference between the center and the wall is

$$\Delta T_n = T_n|_{x=0} - T_n|_{x=L} = \frac{1}{2} \frac{\dot{Q} L^2}{k_n}. \quad (14)$$

For a power density deposited in the plasma of 0.25 W/cm^3 and assuming that 20% of the power is consumed in gas heating, $\dot{Q} = 0.05 \text{ W/cm}^3$, and the gas temperature difference is only $\Delta T_n \sim 5 \text{ K}$, for $L \sim 5 \text{ mm}$. In addition, for the relatively high pressures considered, the temperature “jump” at the wall (the difference between the gas temperature at the wall and the wall temperature itself) is negligible. This indicates that neutral gas heating should not be important for miniaturized plasma reactors (small L), even for relatively high power densities deposited in the plasma. Consequently, the effect of neutral gas heating was not included in the simulation.

III. METHOD OF SOLUTION

The set of nonlinear coupled partial differential equations for T_e , and species transport [Eqs. (6), (8) and (10)] was spatially discretized using a Streamline Upwind Petrov–Galerkin method¹⁶ to yield a system of equations of the form

$$\mathbf{A}(\mathbf{u}) \dot{\mathbf{u}} = \mathbf{K}(\mathbf{u}) \mathbf{u} + \mathbf{F}(\mathbf{u}), \quad (15)$$

where \mathbf{u} represents the solution vector, $\dot{\mathbf{u}}$ is the time derivative of \mathbf{u} , and \mathbf{A} and \mathbf{K} are banded nonlinear mass and stiffness matrices, respectively. \mathbf{F} is a nonlinear source vector. The resulting set of implicit ordinary differential equations in Eq. (15) was integrated in time using backward difference Formulas¹⁷ until a steady state was obtained. At each time step, the equation for the azimuthal electric field [Eq. (1)] was solved using the Galerkin finite element method and a

TABLE III. Species mobility and diffusivity (from Ref. 9, N is gas density).

Name	Symbol	Value
Ar ⁺ mobility	$N\mu_+$ (cm ⁻¹ V ⁻¹ s ⁻¹)	4.65 10 ¹⁹
Ar* diffusivity	ND_k (cm ⁻¹ s ⁻¹)	2.42 10 ¹⁸

direct band solver. The convergence criterion was set by evaluating the L^2 norm of the solution normalized with respect to the average i.e.,

$$\epsilon_j = \frac{1}{V^{1/2}} \left[\int_{\Omega} \left\{ \left(\frac{u_j}{\langle u_j \rangle} \right)_{(i+1)} - \left(\frac{u_j}{\langle u_j \rangle} \right)_i \right\}^2 d\Omega \right]^{1/2}, \quad (16)$$

where, for each variable j , ϵ_j , u_j , and $\langle u_j \rangle$ are a tolerance parameter, value of that variable (e.g., ion density), and its average, respectively, over the domain of interest Ω . V is the plasma volume, and i is the iteration number ($i=1,2,3,\dots$). The convergence criterion was tested after each iteration. Integration was terminated when the evaluated tolerance was less than a user-specified value (0.5%) for all species density and electron temperature.

IV. RESULTS AND DISCUSSION

An argon discharge was simulated in the mICP of Fig. 1 under the base case parameters shown in Table II. The ion mobility and metastable diffusivity are shown in Table III at 300 K.⁹ The ionic diffusivity was computed using the Einstein relation $D_i = \mu_i k_B T_i / e$, where T_i is the ion temperature.

The power deposition profile (in W/cm³) is shown in Fig. 2. Power is deposited directly under the coil in a toroidal pattern, with a typical skin depth of ~1 mm at the high frequency of 450 MHz. The max power density is ~0.66 W/cm³ for a total power of 0.0325 W (1.3 W at 2.5% efficiency) absorbed by the plasma.

Figure 3 shows the electron temperature profile. The electron temperature is highest (~2.7 eV) near the maximum of power deposition (see Fig. 2). Despite the fact that power

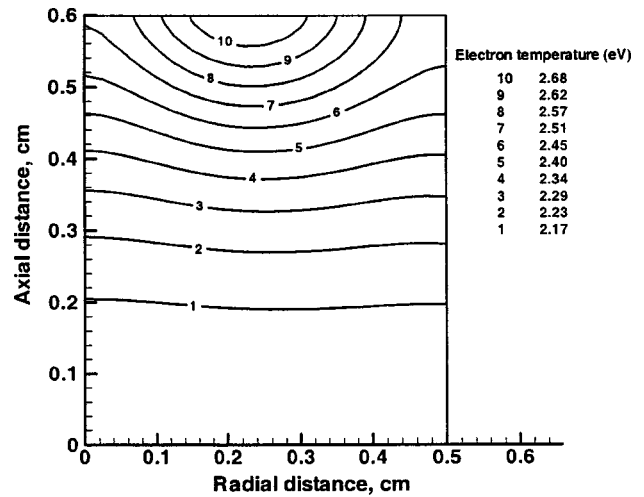


FIG. 3. Electron temperature profile under the base case conditions of Table II.

is deposited in a small toroidal zone under the coil, electrons are substantially warm throughout the reactor due to the high thermal conductivity of the electron gas (the electron thermal conductivity is proportional to the electron density). Lower pressures would lead to higher electron temperatures and more uniform temperature distributions.

The ion density profile is shown in Fig. 4. The peak ion density is on axis at ~6.5 × 10¹⁰ cm⁻³. The peak ion density is located above the axial midplane since power is deposited only near the upper boundary of the plasma. The ion density drops by an order of magnitude (from the peak value) at the sheath edge due to the relatively high gas pressure. The ion density gradients are rather severe and point to a possible difficulty in trying to make spatially resolved measurements in miniature plasma reactors. For example, the ion density can vary by a factor of more than 5 over a distance of 1 mm, see for example the density gradient at $R=0$ between $z=0.5$ mm and $z=0.6$ mm in Fig. 4. Thus, a Langmuir probe will measure only an average ion density over the active length of the probe.

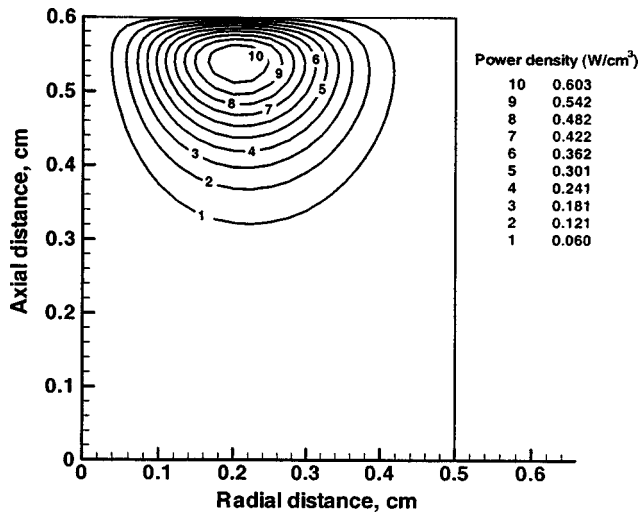


FIG. 2. Inductive power deposition profile under the base case conditions of Table II.

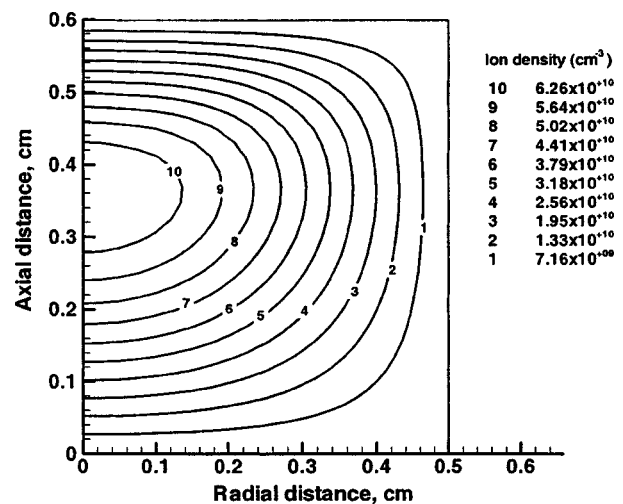


FIG. 4. Ion density profile under the base case conditions of Table II.

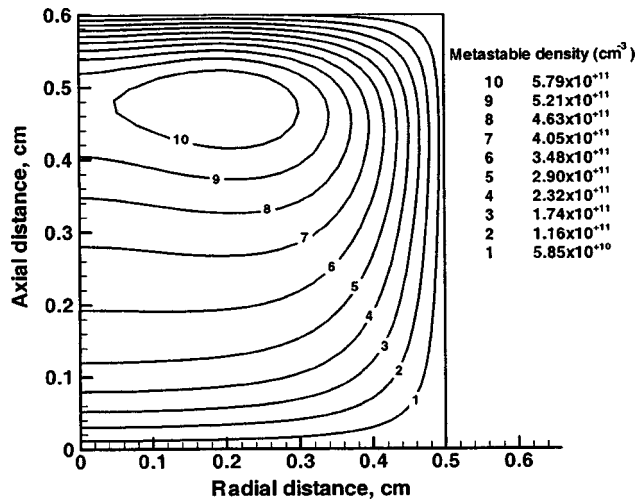


FIG. 5. Metastable density profile under the base case conditions of Table II.

The metastable density profile is shown in Fig. 5. The metastable density peaks off axis closer to the upper boundary compared to the ion density profile. This is due to reaction R4 of Table I destroying metastables. The destruction rate is proportional to the electron density (equal to the ion density in the bulk plasma). The metastable density drops by more than an order of magnitude (from the peak value) close to the walls as metastables are destroyed with 100% probability at the walls.

A. Comparison with experimental data

Figure 6 shows a comparison of simulation predictions with experimental data¹ of ion density as a function of pressure. The Langmuir probe data were obtained at $R=0$, $z=0.5$ mm. The total power delivered to the plasma was 1.3 W. However, in such mICPs, the power absorption efficiency f is only a few percent for pressures below 1 torr.¹⁸ The simulation results shown in Fig. 6 (and also Figs. 7 and 8 below) were computed using $f=0.025$ (2.5% efficiency). The ion density increases linearly with pressure over the limited range (370–770 mtorr) examined.

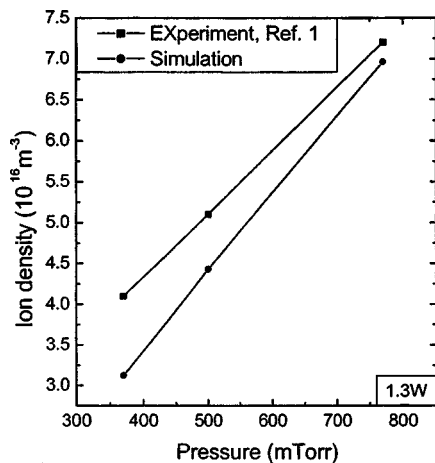


FIG. 6. Comparison between simulation predictions (dots) and experimental data (squares) of ion density for different pressures at a power of 1.3 W. Lines are drawn to guide the eye.

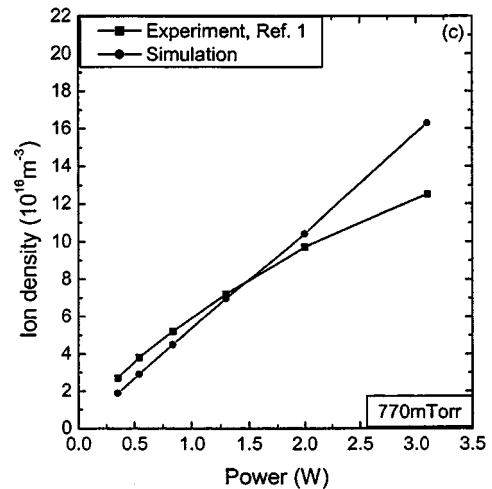
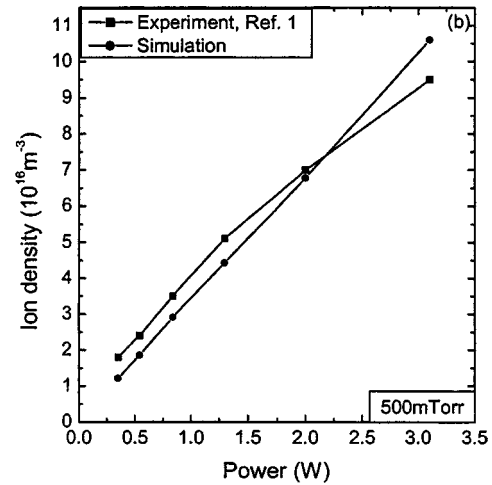
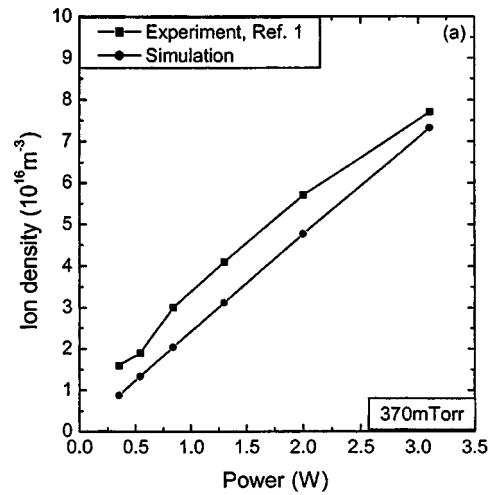


FIG. 7. Comparison between simulation predictions (dots) and experimental data (squares) of ion density as a function of power for (a) 370 mtorr, (b) 500 mtorr, and (c) 770 mtorr. Lines are drawn to guide the eye.

Figures 7(a)–7(c) shows a comparison of simulation predictions with experimental data¹ as a function of power for three different pressures. The simulation predicts a linear dependence of ion density with power as would be expected for ICPs, and is in reasonable agreement with the data over the whole range of powers and pressures. The crossover between simulation predictions and data in Figs. 7(b) and 7(c) may be

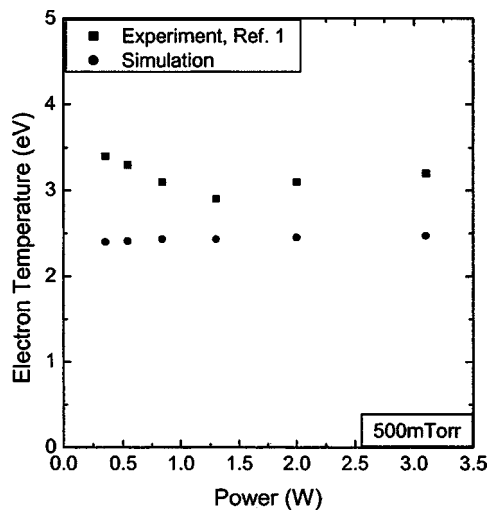


FIG. 8. Comparison between simulation predictions (dots) and experimental data (squares) of electron temperature as a function of power for 500 mtorr. Lines are drawn to guide the eye.

due to the fact that the power absorption efficiency was kept constant in the simulation. In practice the power absorption efficiency increases with pressure and decreases with power.¹⁸ The limited spatial resolution of the Langmuir probe (see discussion in connection with Fig. 4 above) may also contribute to the discrepancies between simulation predictions and measurements.

Finally, Fig. 8 shows the measured electron temperature¹ compared to simulation predictions as a function of power for a pressure of 500 mtorr. The simulation predicts T_e independent of power, about 0.5 eV lower than the measurements. Possible reasons for the differences are (a) the actual electron energy distribution function may differ from Maxwellian, and (b) accurate electron temperature measurements with Langmuir probes are known to be very challenging.^{19,20} This is especially true in microsystems in which the electron current to the probe is limited by the ion current flowing to the (very small surface area) system walls.

V. CONCLUSIONS

A two-dimensional simulation of a miniaturized cylindrical (5 mm radius, 6 mm length) inductively coupled plasma (mICP) reactor was developed. An equation for the azimuthal electric field was solved to calculate the inductive power deposition. The latter was coupled self-consistently to the plasma transport equations to compute the spatial structure of the discharge. The electron temperature was found to

peak in the region of power deposition (under the coils). Considerably warm electrons persisted away from the power deposition zone due to the relatively high thermal conductivity of the electron gas. Strong ion density gradients were observed which can make spatially resolved Langmuir probe measurements particularly challenging. The neutral gas temperature is expected to be only a few degrees above the wall temperature due to efficient heat transfer in the small length scale system. Simulation results on ion (electron) density and temperature as a function of power and pressure were in reasonable agreement with experimental data.

ACKNOWLEDGMENTS

Financial support by NSF CTS-0072854 and NSF CTS-0227232 is gratefully acknowledged. Many thanks to Dr. Olga Minayeva and Professor J. Hopwood of Northeastern University for sharing data prior to publication.

- ¹J. Hopwood, O. Minayeva, and Y. Yin, *J. Vac. Sci. Technol. B* **18**, 2446 (2000).
- ²O. B. Minayeva and J. A. Hopwood, *J. Anal. At. Spectrom.* **17**, 1103 (2002).
- ³K. H. Schoenbach, A. El-Habachi, W. Shi, and M. Ciocca, *Plasma Sources Sci. Technol.* **6**, 468 (1997).
- ⁴M. Kurihara and T. Makabe, *IEEE Trans. Plasma Sci.* **27**, 1372 (1999); Y. Ikeda, K. Suzuki, H. Fukumoto, M. Shibata, M. Ishigaki, J. P. Verboncoeur, P. J. Christenson, and C. K. Birdsall, *J. Appl. Phys.* **89**, 4231 (2001).
- ⁵P. Siebert, G. Petzold, A. Hellenbart, and J. Muller, *Appl. Phys. A: Mater. Sci. Process.* **67**, 155 (1998).
- ⁶J. Hopwood, C. R. Guarnier, S. J. Whitehair, and J. J. Cuomo, *J. Vac. Sci. Technol. A* **11**, 152 (1993).
- ⁷B. Ramamurthi and D. J. Economou, *Plasma Sources Sci. Technol.* **11**, 324 (2002).
- ⁸S.-K. Nam, C. B. Shin, and D. J. Economou, *Mater. Sci. Semicond. Process.* **2**, 271 (1999).
- ⁹D. P. Lymberopoulos and D. J. Economou, *J. Appl. Phys.* **73**, 3668 (1993).
- ¹⁰V. I. Kolobov and D. J. Economou, *Plasma Sources Sci. Technol.* **6**, 1 (1997).
- ¹¹B. Ramamurthi, D. J. Economou, and I. Kaganovich, *Plasma Sources Sci. Technol.* **12**, 170 (2003).
- ¹²E. F. Jaeger, L. A. Berry, J. S. Tolliver, and D. B. Batchelor, *Phys. Plasmas* **2**, 2597 (1995).
- ¹³T. Panagopoulos, V. Midha, D. Kim, and D. J. Economou, *J. Appl. Phys.* **91**, 2687 (2002); V. Midha and D. J. Economou, *J. Electrochem. Soc.* **144**, 4062 (1997).
- ¹⁴P. J. Chantry, *J. Appl. Phys.* **62**, 1141 (1987).
- ¹⁵G. A. Hebner, *J. Appl. Phys.* **80**, 2624 (1996).
- ¹⁶A. N. Brooks and T. J. R. Hughes, *Comput. Methods Appl. Mech. Eng.* **32**, 199 (1982).
- ¹⁷G. D. Byrne and A. C. Hindmarsh, *J. Comput. Phys.* **70**, 1 (1987).
- ¹⁸O. B. Minayeva and J. Hopwood, *J. Appl. Phys.* **94**, 2821 (2003).
- ¹⁹V. Godyak, R. Piejak, and B. Alexandrovich, *Plasma Sources Sci. Technol.* **1**, 36 (1992).
- ²⁰P. A. Miller, G. A. Hebner, K. E. Greenberg, P. D. Pochan, and B. P. Aragon, *J. Res. Natl. Inst. Stand. Technol.* **100**, 427 (1995).